Synthetic Aperture Radar Imaging Using Spectral Estimation Techniques

Shivakumar Ramakrishnan
Vincent Demarcus
Jerome Le Ny
Neal Patwari
Joel Gussy

University of Michigan
EECS 559 - Advanced Signal Processing
10 Apr 02

I. Introduction

Synthetic Aperture Radar (SAR) imaging has had an impact in many disciplines over the past few decades. The high quality images taken from satellites and aircraft, initially designed for military surveillance and target detection, have been applied to make advances in accurate mapping, geological exploration, environmental monitoring, and agriculture. Satellite and airborne SAR data has become readily available in the past decade, and processing of the data has become key. Traditional FFT-based methods to process signal and phase history data into images are widely used, even though they suffer from poor resolution and high sidelobe artifacts. However, modern spectral estimation methods provide an attractive alternative that can improve resolution, help eliminate image speckle effects, and increase the accuracy of interferometric height estimates. These methods promise to improve the clarity and applicability of SAR imaging for many applications.

This project set out to explore various spectral estimation techniques that can be applied to SAR imaging systems. In Section II, we show how SAR imaging systems record data that has a Fourier Transform relationship with the image that we want to measure. In Section III, we show how to apply spectral estimation techniques learned in class and in the literature [1-3] to two dimensions. In Section IV, we study the performance of SAR imaging methods in simulations using computer-generated SAR data. Then, in Section V, we evaluate the performance of each method visually using simulated SAR images in the presence of additive noise and phase errors. Finally, actual SAR data was used with our algorithms to judge the effect of the implemented algorithms on real SAR systems.

II. Background: Spotlight Synthetic Aperture Radar

The goal of the SAR imaging system is to produce an estimate of the amplitude of the reflectivity function $g(x,y)$ of a scene. In this section, we show how illuminating the scene using radar produces phase history data that has a two-dimensional Fourier Transform relationship with $g(x,y)$. The main goal of this project is to study the power spectral estimation problem of converting the phase history to an image. However, it is important to gain a physical understanding of the measurement process that produces the phase history to justify the mathematical model used and to be able to generate test data for our simulations.

In the SAR system, the antenna is fixed to an aircraft flying in the *cross-range or azimuth direction*, and the beam looks out from the side of the aircraft, in the direction referred to as the *range direction*. As the aircraft moves along its flight path, it periodically transmits pulses of microwave energy that are reflected back by the targets on the ground and received by the radar [11]. The data collected is called the phase history, which is passed to a processor. Figs. 1 and 2 show an SAR system and explain the notations used throughout this section.

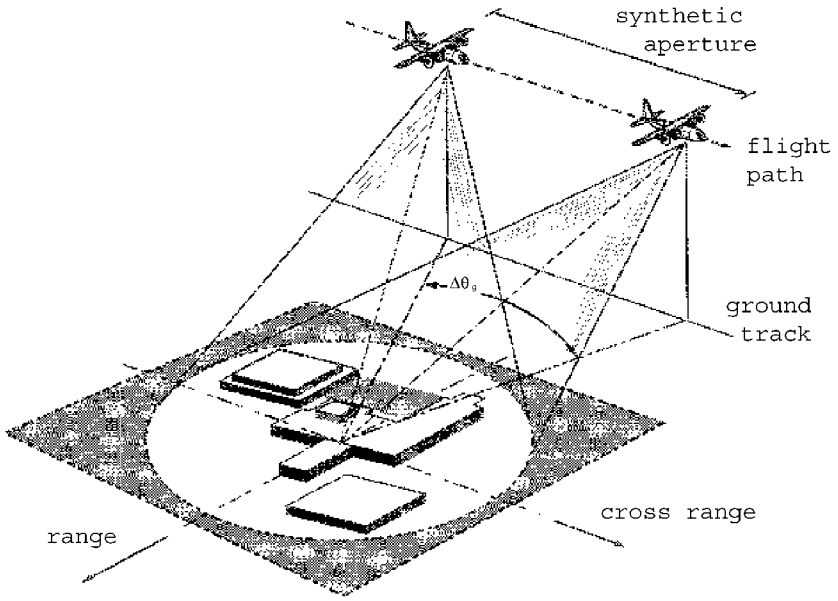

Figure 1. Spotlight mode synthetic aperture radar. The radar is steered continually during the flight. [11]

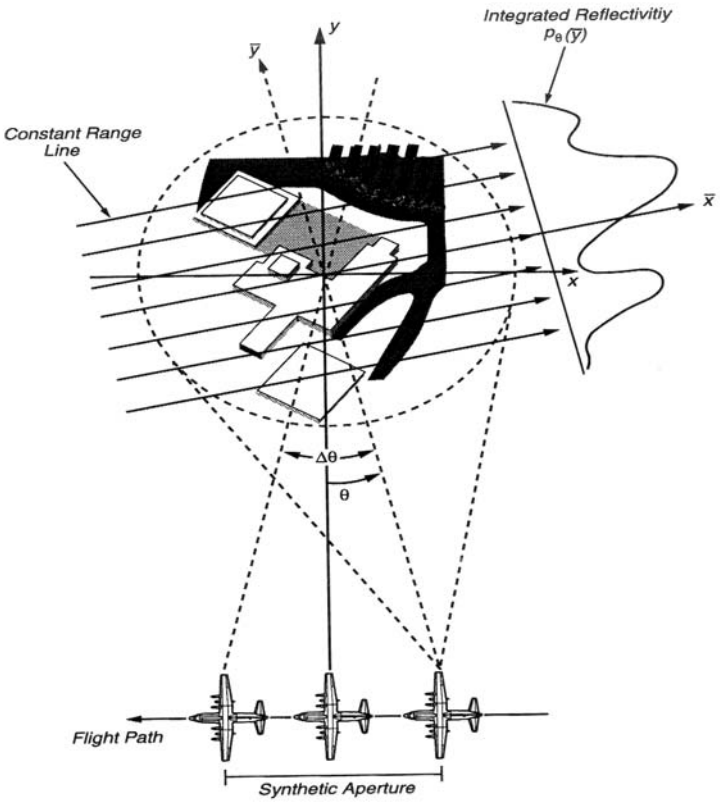

Figure 2. SAR principle. The data received in each pulse is the reflectivity integrated over a wave front $y = y_1$. [11]

A SAR system launches spherical wave fronts, but because the radar platform typically operates at standoff distances that are large compared to the scene diameter, these wave fronts are well approximated as planar. The receiver measures the signals reflected by all targets lying along the same constant-range contour at the same time. Thus the measured signal is not simply the value of the complex reflectivity function at any one ground position (x,y). Instead, the receiver integrates the reflectivity values from all targets that lie along the corresponding constant ground range line $y = y_1$. The SAR system resolves the ambiguity by using information from the other times that the target is illuminated as the aircraft moves along its flight path [11]. The longer the target is illuminated, the more information we can get on the position.

Two different principal modes are used in SAR imaging:

1. In the *strip-map mode*, the antenna is aimed orthogonal to the flight path and keeps this orientation
2. When better resolution for a smaller ground patch is desired, the *spotlight mode* is preferred. In this mode, the illuminating radar beam is steered continually as the aircraft moves, so that it illuminates the same patch over a longer period of time.

In this project, we restrict our analysis to the latter technique. Processing of the phase history generated in spotlight mode requires 2-D power spectral estimation methods for image formation, which is the motivation for our project.

1. Range Compression

The signal emitted by the radar is usually a linear FM chirp [11] described by $Re\{s(t)\}$, with

(Eq. 1) $$s(t) = \begin{cases} \exp\left[j\left(\omega_0 t + \alpha t^2\right)\right] & -\tau_c/2 \le t \le \tau_c/2 \\ 0 & otherwise \end{cases}$$

The frequencies encoded by the chirp $s(t)$ extend from $\omega_0 - \alpha\,\tau_c$ to $\omega_0 + \alpha\,\tau_c$. We assume that the ground patch illuminated extends to the area $(x, y) \in [-L, L] \times [-L, L]$. Then with the notations defined in Fig. 1, the return signal is expressed as:

(Eq. 2) $$r_c(t) = A\ \mathrm{Re}\left\{ \int_{-L}^{L} p_\theta(\bar{y}) \exp\left\{ j\left[\omega_0\left(t - \tau_0 - \bar{\tau}\bar{y}\right) + \alpha\left(t - \tau_0 - \bar{\tau}\bar{y}\right)^2 \right] \right\} d\bar{y} \right\}$$

with

(Eq. 3) $$p_\theta(\bar{y}) = \int_{-L}^{L} g\left(\bar{x}\cos\theta - \bar{y}\sin\theta, \bar{x}\sin\theta + \bar{y}\cos\theta\right) d\bar{x}$$

(Eq. 4) $$\tau_0 = \frac{2R}{c},\ \tau = \frac{2\bar{y}\cos\psi}{c}$$

where R is the distance to the center of the ground patch, and $\bar{x}$ and $\bar{y}$ are given by the linear transformation,

(Eq. 5) $$\bar{x} = x\cos\theta + y\sin\theta$$

(Eq. 6) $$\bar{y} = -x\sin\theta + y\cos\theta$$

Note that we introduce the *depression angle* ψ, i.e. the angle that the incident microwave makes with the ground, and c, the speed of light.

The first task is to remove the effect of the carrier from $r_c(t)$. We will then show that the collection of functions $p_\theta(\bar{y})$ obtained over an interval of viewing angles, $\Delta\theta$, contains sufficient information to reconstruct $g(x,y)$.

The equation for $r_c(t)$ can be interpreted as the convolution of p_θ and the signal s, with the output evaluated at $t+\tau_0$, where τ_0 is the delay of the wavefront received form $y=0$ (the middle line of the illuminated ground patch). We define the patch propagation time τ_p as the difference in two-way propagation delay between a target at the near-edge and a target at the far-edge of the illuminated patch ($\tau_0 = 4L\cos\psi/c$). Then we can see that the equation for $r_c(t)$ is valid only for times that are in the common intersection of the return from near-edge and far-edge targets. This restricts the processing window to the common time segment for which chirp returns from all targets in the ground patch exist simultaneously:

(Eq. 7) $$\tau_0 + \frac{\tau_p}{2} - \frac{\tau_c}{2} \le t \le \tau_0 - \frac{\tau_p}{2} + \frac{\tau_c}{2}$$

In our case, we take $\tau_c >> \tau_p$, and then there is an attractive technique which can be used to deconvolve $s(t)$ from $r_c(t)$, called *deramp processing*. This is accomplished in three steps:

1) Mixing the returned signal with the delayed in-phase and quadrature versions of the transmitted FM chirp;
2) Low-pass filtering the mixer output; and
3) Fourier transforming the low-passed signal.

We give the mathematical analysis of these steps in the following.

<u>Mixing</u>

The mixing step requires that we know the round-trip propagation time τ_0 to the center of the ground patch; this is determined by electronic navigation systems, and imperfections on this value makes it necessary to have additional post-processing techniques. The deramp mixing terms are given by:

(Eq. 8) $$c_I(t) = \cos(\omega_0(t-\tau_0) + \alpha(t-\tau_0)^2)$$
$$and \quad c_Q(t) = -\sin(\omega_0(t-\tau_0) + \alpha(t-\tau_0)^2)$$

By multiplying $r_c(t)$ with the first signal, one can show that we obtain the following expression:

$$\bar{r}_{cI}(t) = \frac{A}{2}\Re\left\{\int_{-L}^{L} p_\theta(\bar{y})\exp\left[j[\omega_0(2t-\tau(\bar{y})-2\tau_0)+\alpha((t-\tau_0)^2+(t-\tau(\bar{y})-\tau_0)^2)]\right] d\,\bar{y}\right\}$$
$$+\frac{A}{2}\Re\left\{\int_{-L}^{L} p_\theta(\bar{y})\exp\left[j[\alpha\tau^2(\bar{y})-\tau(\bar{y})(\omega_0+2\alpha(t-\tau_0))]\right] d\,\bar{y}\right\}$$

Low-Pass Filtering

We see that we can remove the first term in the previous expression with a low-pass filter. We do this to remove the part of the signal centered at frequency $2\omega_0$ and to extract the baseband signal. We proceed in a similar way with the quadrature component, to get the signals:

(Eq. 9) $$r_{cI}(t) = \frac{A}{2}\Re\left\{\int_{-L}^{L} p_\theta(\bar{y})\exp\left\{j\left[\alpha\tau^2(\bar{y})-\tau(\bar{y})(\omega_0+2\alpha(t-\tau_0))\right]\right\}d\bar{y}\right\}$$

(Eq. 10) $$r_{cQ}(t) = \frac{A}{2}\Im\left\{\int_{-L}^{L} p_\theta(\bar{y})\exp\left\{j\left[\alpha\tau^2(\bar{y})-\tau(\bar{y})(\omega_0+2\alpha(t-\tau_0))\right]\right\}d\bar{y}\right\}$$

(Eq. 11) $$r_c(t) = r_{cI}(t) + jr_{cQ}(t) = \frac{A}{2}\left\{\int_{-L}^{L} p_\theta(\bar{y})\exp\left\{j\left[\alpha\tau^2(\bar{y})-\tau(\bar{y})(\omega_0+2\alpha(t-\tau_0))\right]\right\}d\bar{y}\right\}$$

Ignoring the quadratic phase term $\alpha\tau^2$ (we could add this effect in a more precise study), we get at the output of the quadrature demodulator:

(Eq. 12) $$r_c(t) = \frac{A}{2}\int_{-L}^{L} p_\theta(\bar{y})\exp\left[-j\frac{2\bar{y}\cos\psi}{c}(\omega_0+2\alpha(t-\tau_0))\right]d\bar{y}$$

Fourier Transforming

We can recognize in the last expression the Fourier transform of p_θ over a certain range of *spatial frequencies.* Plugging the interval on which the signal is processed (Eq. (7)), we conclude that the Fourier transform is determined over the interval of spatial frequencies $Y = (2/c)\cos\psi(\omega_0+2\alpha(t-\tau_0))$ given by (with $\tau_c >> \tau_p$):

(Eq. 13) $$\frac{2\cos\psi}{c}(\omega_0-\alpha\tau_c) \le Y \le \frac{2\cos\psi}{c}(\omega_0+\alpha\tau_c)$$

And thus a final Fourier transformation (also called range compression) of $r_c(t)$ gives the estimate of $p_\theta(\bar{y})$.

2. Cross-Range Resolution Problem

Now that we have recovered $p_\theta(\bar{y}) = \int_{-L}^{L} g(\bar{x}\cos\theta - \bar{y}\sin\theta, \bar{x}\sin\theta + \bar{y}\cos\theta)d\bar{x}$

for $\bar{y}$ in $[-L, L]$ and θ describing an interval $\Delta\theta$, we still have to show that we can extract from it an estimate of the reflectivity function $g(x,y)$. The Projection-Slice

theorem states that the 1D Fourier transform of any projection function $p_\theta(u)$ is equal to the 2D Fourier transform $G(X,Y)$ of the image to be reconstructed (i.e. the reflectivity function) evaluated along a line in the Fourier domain that lies at the same angle θ measured from the X axis [11]. That is:

(Eq. 14)
$$G(U\cos\theta, U\sin\theta) = \int_{-\infty}^{\infty} p_\theta(u) e^{-juU}\, du = P_\theta(U)$$
$$where \quad G(X,Y) = \int_{-\infty}^{\infty}\int_{-\infty}^{\infty} g(x,y) e^{-j(xX+yY)}\, dxdy$$

Note that the finite limits $-L$ and L can be used here because g is zero outside the circle centered at the origin with radius L. This result is easily shown using a rotational change of variable:

(Eq. 15)
$$\begin{bmatrix} x \\ y \end{bmatrix} = \begin{bmatrix} \cos\theta & -\sin\theta \\ \sin\vartheta & \cos\theta \end{bmatrix} \begin{bmatrix} \bar{x} \\ \bar{y} \end{bmatrix}$$

in the expression of $G(U\cos\theta, U\sin\theta)$.

Therefore, we see that starting from the projection functions $p_\theta(\bar{y})$ over a range of θ, we can determine the values of the two-dimensional Fourier transform $G(X,Y)$ along lines of the same orientation by taking the one-dimensional Fourier transform of $p_\theta(\bar{y})$. If the projections span 180° of viewing directions, we can then obtain the complete Fourier transform $G(X,Y)$ of the reflectivity function in a circular region. In practice, the projections are taken for a discrete set of angles θ and positions $\bar{y}$. Thus we can obtain a reconstructed image $g(x,y)$ by simply taking the discrete inverse Fourier transform of the data. However, as we have seen, these data are organized in a way that is compatible with a polar coordinate system, and in practice, we must first perform a polar to Cartesian coordinates interpolation in order to use the FFT algorithm. A more precise description of this transformation can be found in [11].

3. Phase history and SAR data

To conclude this section of the SAR imaging system, we sum up the results that justify the study that we will conduct in the following sections. In this report, we use the *phase history*, that is, SAR data in its final form after the Cartesian to polar interpolation. From the results of this section, we know that applying a 2D-FFT on this phase history will furnish an estimate of the reflectivity function $g(x,y)$. Thus, this complicated data acquisition process can be exploited very simply in this project.

These characteristics of the spotlight mode SAR data show clearly why spectral estimation techniques are useful. As an example, a single scatterer at point (x,y) with reflectivity amplitude of α will generate a phase history of the form:

$$\phi = \left(\alpha e^{j(nx+my)}\right)_{0\le n\le N,\,0\le m\le M} \qquad \text{(Eq. 16)}$$

Note that this result is after sampling and ignoring the phase terms since we are only interested in the amplitude. Fig. 1 shows the phase history generated by just one point; considering an image as a discrete set of points, we will just need to add these functions to generate the final phase history. A single point scatterer results in a two dimensional sinusoid but only a finite set of samples. Therefore by replacing the 2D-FFT with refined spectral estimation methods, we hope to increase the quality of the reconstructed *spatial spectrum*.

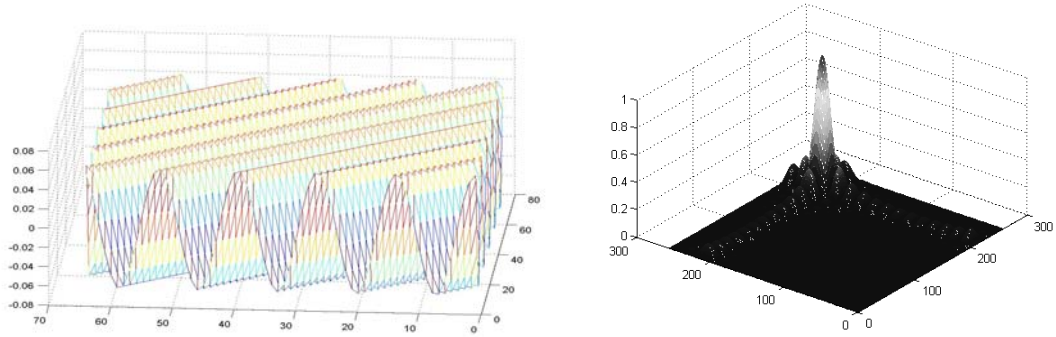

Figure 3. Point target phase history (real part) and 2D FFT Reconstruction

The following sections will present some possible techniques based on well-known one-dimensional algorithms, and evaluate their performance for SAR image reconstruction.

III. Spectral Estimation Techniques

We chose to implement several spectral estimation methods in order to gain an understanding of the SAR imaging problem. From non-parametric methods, we implemented a baseline FFT method, several Periodogram-based methods, including the Windowed Periodogram, Blackman-Tukey and Welch methods as well as the Capon and APES methods. We also implemented the EigenVector (EV) method, which is a parametric subspace decomposition method.

In looking at the formulations for each method, it became apparent that each method would provide different magnitudes when applied to our data. For example, we know for the Capon method that different normalization methods exist, and there is no absolute justification for them. Since we were interested in evaluating image quality and not necessarily in evaluating peak intensities, we did not develop elaborate normalization schemes for each method. In the actual

MATLAB implementations, we chose to simply normalize each method by its peak level and display on a dB scale.

In addition, we normalized the units of the results. Since the FFT is an estimate of amplitude, while all other methods are estimates of power, there is a discrepancy in the results unless we normalize one or the other. Since we use the FFT as our baseline, we chose to take the square root of the output of all methods except for the FFT. (We could have chosen to square the FFT and leave the others alone, but the choice was arbitrary). Since our images are displayed on a dB scale, the square root operation does affect the range, but doesn't change the image otherwise.

1. FFT

To establish an initial image, a 2-D FFT was applied to the phase history data. As mentioned, this image was used as a baseline for comparing the results of the spectral estimation techniques described below. Note that in practice, the FFT and the Windowed Periodogram are the most common methods used for generating SAR images.

2. Periodogram based Methods

The first spectral estimation methods studied were the Periodogram based methods, namely, the Windowed Periodogram, Blackman-Tukey, and Welch methods. These can be thought of as refined versions of the FFT and were simple to implement.

Windowed Periodogram

The windowed Periodogram was the first spectral estimation technique evaluated. A two-dimensional discrete space extension of the 1-D case described in [2] was derived. The resulting formula was found to be:

$$\hat{\phi}_p(\omega_x,\omega_y) = \frac{1}{MN}\left|\sum_{m=0}^{M-1}\sum_{n=0}^{N-1} v(n,m)\,y(n,m)e^{-j(\omega_x n+\omega_y m)}\right|^2 \qquad \text{(Eq. 17)}$$

where $v(n,m)$ is a 2-D window function, and $y(n,m)$ is the two-dimensional phase history of size $[NxM]$. Here, ω_x and ω_y are frequencies that correspond to point (x,y) of the image. This formula was implemented in MATLAB using a 2-D FFT. For this implementation, the window size was chosen to be equal to the phase history size. In this case, choosing a rectangular window function is equivalent to the 2-D un-windowed Periodogram. Of the variety of window functions available for use in the windowed Periodogram, a Taylor window was chosen. A Taylor window is commonly used in SAR imaging because it provides strong sidelobe reductions

with minimal effect on resolution [6]. Additionally, the sidelobe reduction is selectable via the window parameters. For this evaluation, the peak sidelobe level was set to –35dB and the number of nearly constant level sidelobes adjacent to the mainlobe was chosen as 5. These are typical SAR parameters. The Taylor window equations were obtained from [6]. The 2-D window was formed by combination of the 1-D window functions in MATLAB.

Blackman-Tukey

The next method studied was the Blackman-Tukey method. This method seeks to improve on the high statistical variance of the spectral estimator as described in [2]. The implementation of this method can be thought of as a locally weighted average of the Periodogram. The 2-D formulation was found to be (here * denotes a convolution)

(Eq. 18) $$\hat{\phi}_{BT}(\omega_x,\omega_y) = \hat{\phi}_p(\omega_x,\omega_y) * V(\omega_x,\omega_y)$$

where $V(\omega_x,\omega_y)$ is the Fourier transform of the window function also referred to as the spectral window. The convolution of this spectral window with the Periodogram estimate results in a smoothing effect in the frequency domain image. While this will theoretically reduce the variance, the resolution is degraded. Careful selection of the window function and its size are necessary to ensure good results. In this case, a Hamming window whose size was one half the final image size was chosen based on subjective assessment of the images. Using MATLAB, the actual application of the window was applied using a 2-D IFFT on the Periodogram estimate, multiplying by the window function and then using a 2-D FFT to obtain the Blackman-Tukey estimate. The Periodogram estimate used here was the un-windowed type as described above.

Welch Method

The final Periodogram based method implemented was the Welch method. This method also seeks to trade resolution for variance through averaging. The 2-D discrete space formulation was found to be:

(Eq. 19)

$$\hat{\phi}_w(\omega_x,\omega_y) = \frac{1}{S_y}\frac{1}{S_x}\sum_{d=1}^{Sy}\sum_{c=1}^{Sx}\frac{1}{M_{S_y}N_{S_x}}\left|\sum_{m=0}^{M_{S_y}-1}\sum_{n=0}^{N_{S_x}-1} v(n,m)y\left[(c-1)K_x+n,(d-1)K_y+m\right]e^{-j(\omega_x n+\omega_y m)}\right|^2$$

In this case, the image is divided into overlapping blocks and averaged together. The terms N_{S_x} and M_{S_y} define the size of each block, and the terms K_x and K_y define the amount of overlap. In this case, the 2-D window $v(n,m)$ is chosen to be the size of each block. The recommended value for K_x and K_y provides for 50%

overlap of each block and is given by is $N/2$ and $M/2$ respectively where N and M are the total phase history size. This is what was used in this study. The S_x and S_y terms define the total number of blocks and is given by the integer parts of $S_x = \frac{(N - N_{s_x} + K_x)}{K_x}$ and $S_y = \frac{(M - M_{s_y} + K_y)}{K_y}$.

3. Covariance-Based Methods

The next spectral estimation methods studied centered on the autocovariance matrix. These methods include the Capon method, EigenVector (EV) method, and the Amplitude and Phase Estimation (APES) method. To use these methods, the first task was to determine the autocovariance matrix.

In two dimensions, the estimation of the autocovariance matrix from the signal history data poses two problems. First, there is no consensus among researchers of which method has the best performance. Secondly, the resulting autocovariance matrix is much larger in this 2-D case than it was in the 1-D case. A 1-D signal length M would result in a correlation matrix size on the order of M. A square image with dimensions MxN would have a autocovariance matrix size the order of (MN), and correspondingly memory requirements on the order of $(MN)^2$. As we attempted to do operations on real phase data of dimensions 256x256, we were limited by the memory available on our computers.

The simplest method used for autocovariance matrix estimation is the covariance method, or sub-aperture averaging [1]. In this method, a small sub-aperture $X_{i,j}$ (a matrix of size K_x by K_y) is chosen from the signal history matrix starting at data point (i,j). Then a vector of length (K_x*K_y) is formed by 'raster scanning', ie., stacking columns of $X_{i,j}$ on top of each other to form a one-dimensional vector, $\underline{x}_{i,j}$. Then, the outer product of $\underline{x}_{i,j}$ is taken, resulting in a autocovariance matrix $R_{i,j}$. This process is repeated for all possible (i,j) and all of the $R_{i,j}$ are averaged together. This produces a 'unidirectional' subaperture estimate R.

The selection of K_x and K_y is up to the user - 40-50% of the data record lengths M and N respectively are recommended by [1], while [7] insists only that $K_x << \mathrm{M}$ and $K_y << \mathrm{N}$ to ensure a sufficient number of lagged products for statistical stability.

A variation of this method is forward-backward subaperture averaging. This method helps average out the noise by using the fact that a 2-D sinusoid evolves in one spatial direction in the same manner as the conjugate sinusoid evolves in the opposite spatial direction [1]. Also, the forward-backward method gives a matrix that is better conditioned than just the forward sample covariance matrix. There are other methods that can be implemented in a computationally less intensive manner - specifically, Toepliz-Block-Toepliz method [8]. However, to ease implementation time, we used forward-backward subaperture averaging in this report.

Capon Method

The Capon method, also called the minimum variance method, is of key importance in high-resolution 2-D spectral estimation. It was originally proposed for 2-D signals [9]. If we define the 2D Fourier vectors as

(Eq. 20) $$W(\omega_x, \omega_y) = \left[1\ e^{-j\omega_X}\ \ldots e^{-j(M-1)\omega_X}\right]^T \otimes \left[1\ e^{-j\omega_y} \cdots e^{-j(M-1)\omega_y}\right]^T$$

(where $\otimes$ denotes the Kronecker product of the two vectors), the amplitude at each point is given by:

(Eq. 21) $$\hat{\phi}_w(\omega_x, \omega_y) = \frac{1}{W^H(\omega_x, \omega_y) R^{-1} W(\omega_x, \omega_y)}$$

The Capon method is designed to pass a 2-D sinusoid at a given frequency without distortion while minimizing the variance of the noise of the resulting image [7]. Calculation of the above equation involves two computationally intensive tasks: inversion of the R matrix, and matrix multiplication by $W(\omega_x, \omega_y)$ vectors, which must be done for each image point.

Subspace Decomposition Methods

The EigenVector (EV) and MUSIC methods are both parametric methods that exploit the assumption that the phase history data is a sum of 2-D sinusoids in a background of white noise. They are called subspace decomposition methods for peak estimation because they separate the eigenvectors of the autocovariance matrix into those corresponding to signals and to clutter. In the EV method, the amplitude of the image at a point (ω_x, ω_y) is given by:

(Eq. 22) $$\hat{\phi}_{EV}(\omega_x, \omega_y) = \frac{1}{W^H(\omega_x, \omega_y)\left(\sum_{clutter} \frac{1}{\lambda_i} \underline{v}_i \underline{v}_i^H\right) W(\omega_x, \omega_y)}$$

while in the MUSIC method, the image amplitude is given by:

(Eq. 23) $$\hat{\phi}_{MUSIC}(\omega_x, \omega_y) = \frac{1}{W^H(\omega_x, \omega_y)\left(\sum_{clutter} \sigma^2 \underline{v}_i \underline{v}_i^H\right) W(\omega_x, \omega_y)}$$

Both methods attempt to bring the denominator to zero when a sinusoidal signal corresponding to a point in the SAR image aligns with one of the signal subspace eigenvectors. At that point, the result is a peak in the image estimate. Thus these methods do not accurately represent the scattering intensity at each point, but

rather show the 'pointiness' of the image. The MUSIC method is considered to be a poor performer in SAR applications [1]. Note that Eq. 22, the EV method uses the inverse of the eigenvalues of the clutter subspace, while in Eq. 23, the MUSIC method uses a constant. The MUSIC method is exploiting further the assumption that clutter is white noise. In practice, this assumption is not entirely true, and the EV method more accurately shows the features of the image. This is why we have chosen to implement the EV method, rather than MUSIC. However, we are not using the EV method to identify particular point scatterers, as we would in a true parametric estimation problem. Instead, we display the normalized amplitude of Eq. 22. As we will see in the results section, this will provide us with a visually appealing result.

Note that if all of the eigenvectors are included in the clutter subspace (model order = 0) the EV method becomes identical to the Capon method. Thus the determination of model order is critical to operation of the EV method. We must decide based on an eigenvalue of the R matrix whether its corresponding eigenvector corresponds to the clutter or to the signal subspace. The number of eigenvectors chosen to be in the signal subspace is called the model order. For our computer-generated SAR data from several point targets in white noise, the eigenvalues corresponding to the different subspaces differ by orders of magnitude. However, in real SAR images, there will be more of a continuum of eigenvalues. One method is to select the model order such that a fixed fraction of the energy is attributed to the signal subspace [1]. Another method is to choose a fixed number for the model order. In our simulations, the EV method model order was chosen to make sure that 98% of the signal energy is included in the signal subspace.

APES Method

The APES method is a matched filter bank method that assumes that the phase history data is a sum of 2-D sinusoids in noise. Empirically, the APES method results in wider spectral peaks than the Capon method, but more accurate spectral estimates for amplitude in SAR [3]. In the Capon method, although the spectral peaks are narrower than the APES, the sidelobes are higher than that for the APES. As a result, the estimate for the amplitude is expected to be less accurate for the Capon method than for the APES method.

The SAR image is estimated using a form similar to the Capon method. Although it uses the forward-backward subaperture averaging autocovariance matrix estimate $\hat{\mathbf{R}}$, the APES method uses it indirectly through another matrix $\mathbf{Q}$, which is another estimate of the covariance matrix. The matrix $\mathbf{Q}$ is given by:

(Eq. 24) $$\mathbf{Q}(\omega_x,\omega_y)=\hat{\mathbf{R}}-\frac{\left[\mathbf{g}(\omega_x,\omega_y)\mathbf{g}^H(\omega_x,\omega_y)+\overline{\mathbf{g}}(\omega_x,\omega_y)\overline{\mathbf{g}}^H(\omega_x,\omega_y)\right]}{(M-K_x+1)(N-K_y+1)}$$

where $\mathbf{g}(\omega_x,\omega_y)=\mathbf{X}_{i,j}\mathbf{W}(\omega_x,\omega_y)$ and $\bar{\mathbf{g}}(\omega_x,\omega_y)=\bar{\mathbf{X}}_{i,j}\mathbf{W}(\omega_x,\omega_y)$. The data matrix $\mathbf{X}_{i,j}$ is the subaperture matrix as defined above and $\bar{\mathbf{X}}_{i,j}$ is the same matrix flipped upside down and left to right. The vector $\mathbf{W}(\omega_x,\omega_y)$ is the K_x by K_y matrix given by:

(Eq. 25) $$\mathbf{W}(\omega_x,\omega_y)=\left[1\; e^{j\omega}\; \ldots\; e^{j(K_x-1)\omega}\right]^T\otimes\left[1\; e^{j\omega}\; \ldots\; e^{j(K_y-1)\omega}\right]^T$$

The constants M, N and K_x, K_y are the dimensions of the full data matrix and the 2-D filter, respectively. The SAR image is then formed as follows:

(Eq. 26) $$\hat{\phi}(\omega_x,\omega_y)=\frac{1}{(M-K_x+1)(N-K_y+1)}\frac{\mathbf{W}^H(\omega_x,\omega_y)\mathbf{Q}^{-1}(\omega_x,\omega_y)\mathbf{g}(\omega_x,\omega_y)}{\mathbf{W}^H(\omega_x,\omega_y)\mathbf{Q}^{-1}(\omega_x,\omega_y)\mathbf{W}(\omega_x,\omega_y)}$$

Note that a matrix inversion, $\mathbf{Q}^{-1}(\omega_x,\omega_y)$, must be calculated for each data point (x,y) of the image. As a result of this requirement, the APES method requires about 1.5 times more computation than the Capon method [10].

IV. Quantitative Analysis of the Techniques on Simulated Data

With the 2-D spectral estimation techniques derived and implemented in MATLAB, it was time to evaluate their performance. The first step in evaluating each method was to develop a set of simulated data. A simple point generation function was developed to create a phase history signal for use in each method. This was based on the theory outlined in Section II. A sample image of a point target is shown below. For the generation of these images, the phase history is zero padded to the desired image size before implementing it with each method. In this case a phase history of 32x32 pixels was used with an image size of 256x256 pixels.

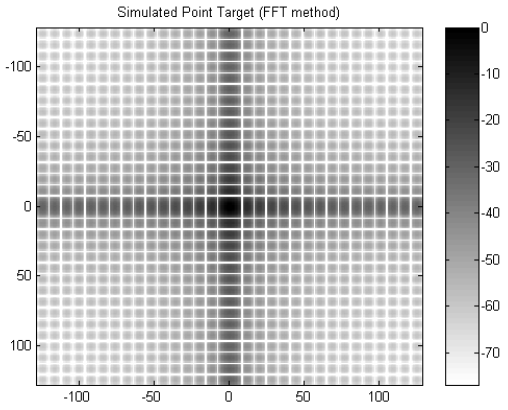

Figure 4. Simulated point target. Image generated via FFT. Note the presence of extensive sidelobes.

As we know from theory, a variety of spectral estimation methods try to trade off noise variance and resolution. In 2-D, this tradeoff still remains, as the results of our simulations show. In this section we determine the spatial resolution of each method presented in Section III. Then, we add various levels of noise into the phase histories in order to judge the noise variance performance.

1. Spatial Resolution

In the first set of simulations, the ability to resolve two closely spaced sources is measured by simulation. Additive noise was set to a very low level in these simulations to attempt to judge the performance of the methods in high SNR situations. (Some level of noise was required to ensure that the covariance matrix was full rank for the Capon, EV, and APES methods.)

In order to determine the resolution of each method, two points were generated a fixed distance apart. A modified Rayleigh resolution criteria was used to determine if the two points were resolved based on determining two distinct peaks down to the –3dB height of the mainlobe. If the points were resolved the distance was reduced and again the routine was run with the reduced distance. The iterations were performed till the smallest distance was achieved for resolution. This method was used to incorporate the effects that adjacent peak sidelobes had on each other. This helped to match the resolution measurements with the subjective assessment in Section V. The results are shown below in Figure 5 (a)-(g).

(a)

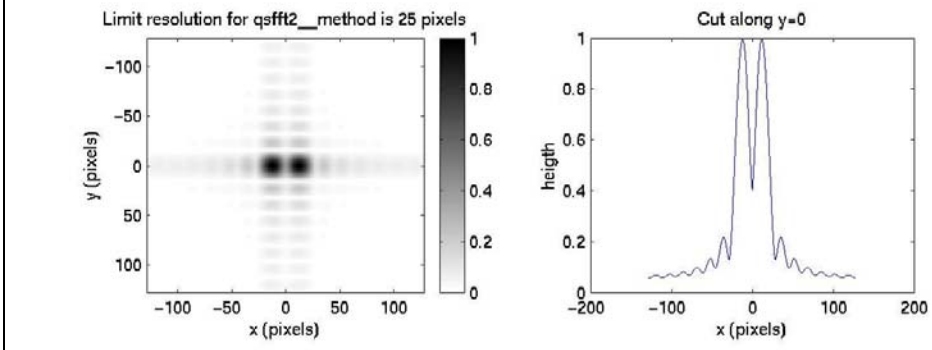

(b)

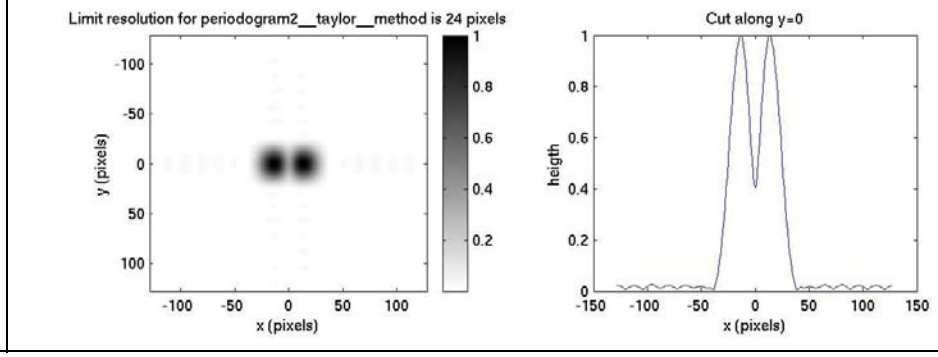

(c)

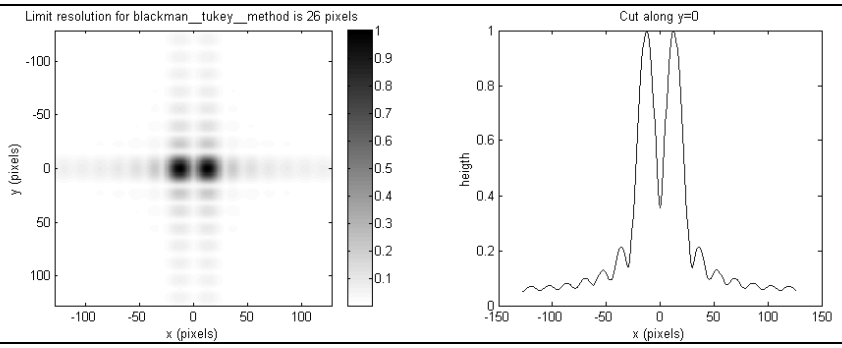
Limit resolution for blackman__tukey__method is 26 pixels
y (pixels)
x (pixels)
Cut along y=0
heigth
x (pixels)

(d)

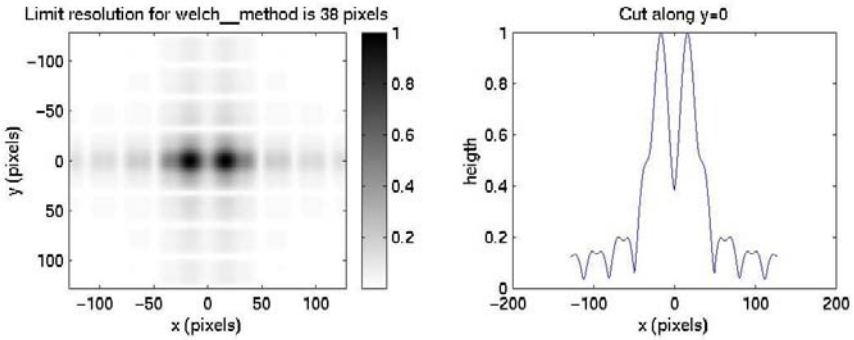
Limit resolution for welch__method is 38 pixels
y (pixels)
x (pixels)
Cut along y=0
heigth
x (pixels)

(e)

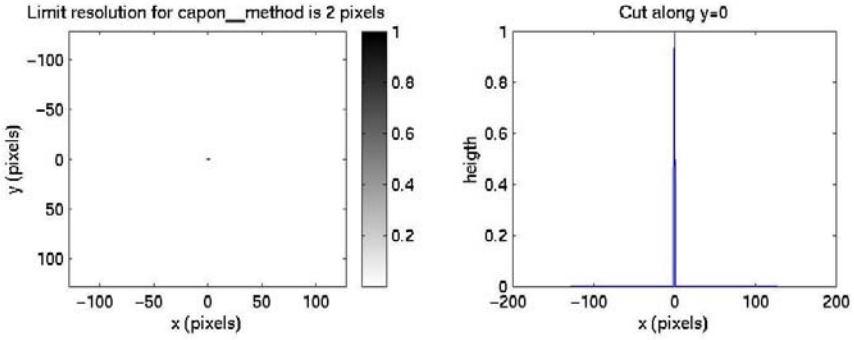
Limit resolution for capon__method is 2 pixels
y (pixels)
x (pixels)
Cut along y=0
heigth
x (pixels)

(f)

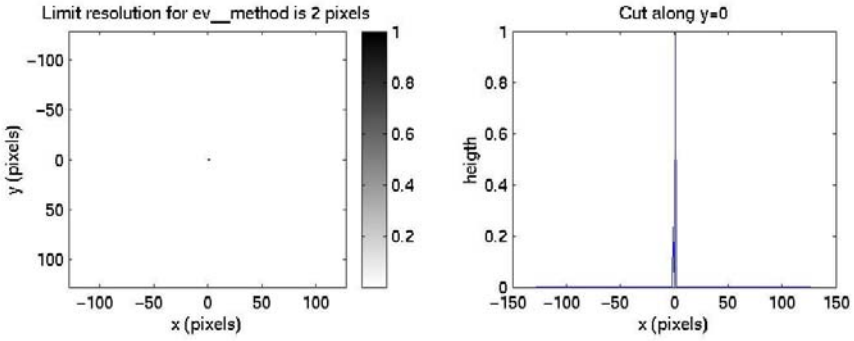
Limit resolution for ev__method is 2 pixels
y (pixels)
x (pixels)
Cut along y=0
heigth
x (pixels)

(g)

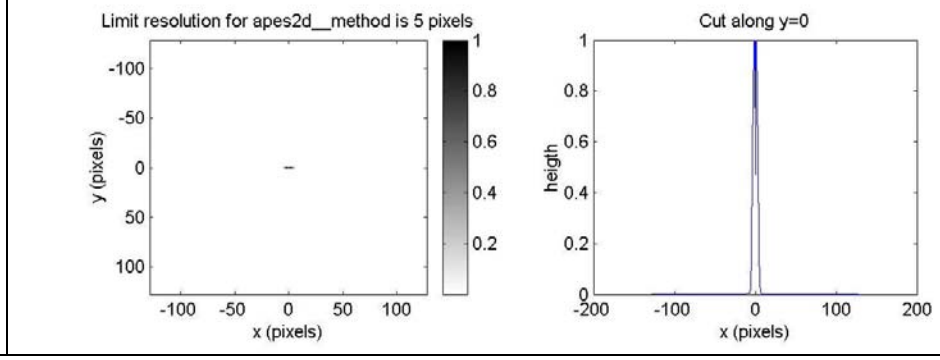

Figure 5. Spatial Resolution Plots: These figures show the 2-D spectral estimation of two point scatterers separated by the resolution limit of the (a) FFT, (b) Taylor-windowed periodogram, (c) Blackman-Tukey, (d) Welch, (e) Capon, (f) EV, and (g) APES methods.

Clearly, the covariance-based methods have significantly higher resolution. As expected, the Welch method performs the worst as it trades resolution for improved variance. This is due to contributions from overlapping blocks inherent in the method. These images and section cuts also provide insight into how each method acts on sidelobes. In this example, the width of the mainlobe and height of the sidelobes contributed to the overall resolution. Table 1 below summarizes the results.

Method	Resolution [pixels]
FFT	25
Windowed Periodogram	24
Blackman Tukey	26
Welch	38
Capon	2
EV	2
APES	5

Table 1: Comparison of Resolution for Various Methods

The Blackman-Tukey appeared nearly identical to the FFT. This is likely due to the large Hamming window whose size was chosen based on subjective image quality. Using a smaller window resulted in less resolution, and a less visually appealing image when using the simulated data described in Section V. Apparently what is considered good to the eye depends more on resolution and less on variance. Both the EV and APES are very similar to the Capon method.

2. Noise Performance

There are two types of noise common to SAR imaging systems, additive and multiplicative. Additive noise typically results primarily from thermal noise from the sensors. Multiplicative noise, on the other hand, is signal dependent, and its overall level is dependent upon the backscatter coefficient of the target [6]. For these reasons, only additive noise was applied to our simulated phase history data

for purposes of evaluation. Circular complex white Gaussian noise was computed with MATLAB in the following manner:

$$noise = \frac{\sigma}{\sqrt{2}}(randn(N,M) + j(randn(N,M))) \quad \text{(Eq. 27)}$$

To illustrate the effects of noise, an example of a point target image is shown below. This is the same point target used in Figure 4. In this case the noise level (σ=0.5) is significant enough to mask many of the sidelobes present in Fig. 4.

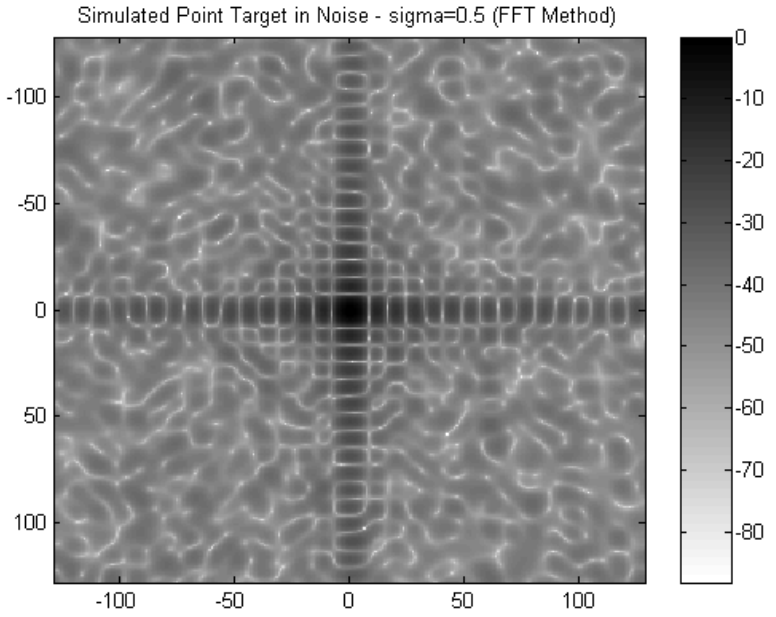

Figure 6. Simulated point target in noise. Image generated via FFT

Mean Squared Error

The MSE of each method in noise is calculated in a series of simulations in which the noise variance varies from 0 to 4 at 13 steps. The MSE calculation was based on a comparison with an image containing the actual points with the estimated image. A total of 100 samples were taken at each noise variance level for each method. Since the MSE measures the bias squared plus the variance, we expect both the bias and noise variance of each method to influence the MSE results, which are are plotted in Fig. 7.

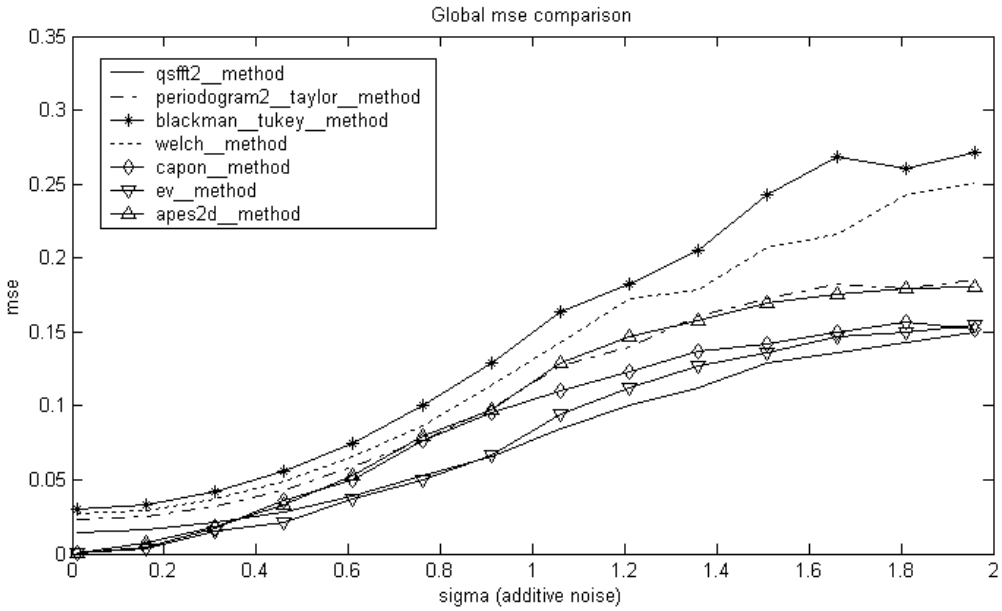

Figure 7. Mean Squared Error (MSE) plotted vs. standard deviation of noise.

This MSE evaluation shows that the Welch and Blackman-Tukey methods performed the worst. This is because the averaging and smoothing effects used by these methods trade bias to reduce variance. The covariance-based methods performed well in low noise conditions, but were surpassed by the FFT at higher noise levels. Of the covariance-based methods, the APES method performed the worst (due to its higher bias) while the EV method was the best. Since it is difficult to separate the influence of the bias and variance in the MSE results, we next performed a separate simulation to study the noise variance of each method.

Signal to Noise Ratio

In this simulation, the phase history was created from a single point scatterer and additive noise. The noise variance was varied from 0 to 4 in 13 increments. Each spectral estimation technique was used to create an output image. In each output image, blocks from each corner were extracted and used to obtain an estimate of the noise variance. This process is illustrated in Fig. 8, where the gray areas are the blocks extracted to estimate the noise. This was done to avoid the sidelobes of the signal peak in the center of the image. For each case, the amplitude of the point target was normalized such that the amplitude in the image was equal to 1. Thus the signal to noise ratio is given simply by:

(Eq. 28) $$SNR = \frac{1}{\hat{\sigma}^2}$$

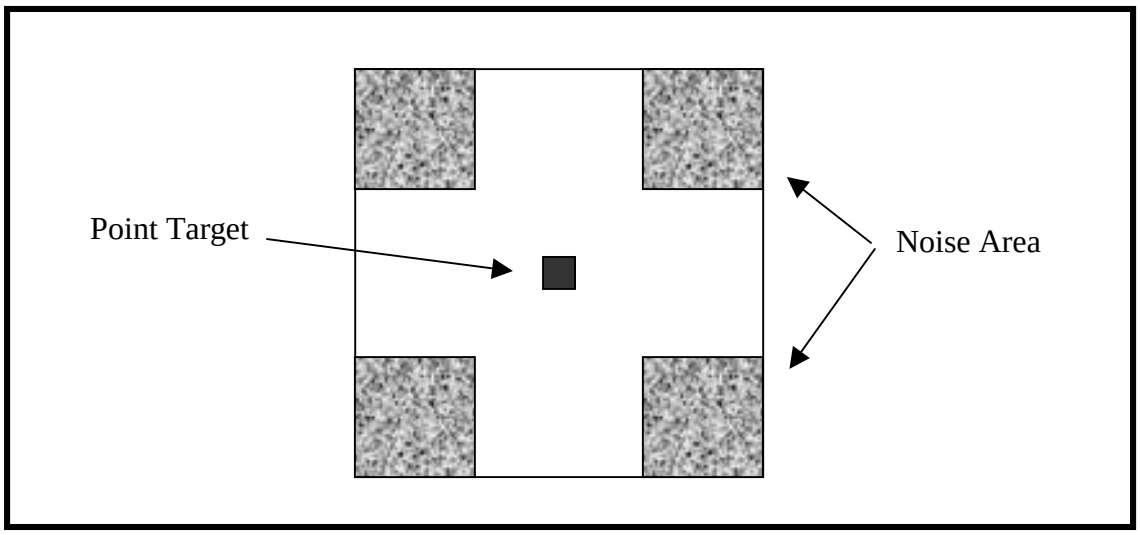

Figure 8. Signal to Noise Ratio (SNR) Measurement Method

The results of the SNR measurements are shown below in Fig. 9. A theoretical prediction of the SNR performance is given for the FFT and Windowed Periodogram methods, and is seen to match the simulations well. For the other methods, analytical results are not as readily obtained, so the simulation results are especially useful.

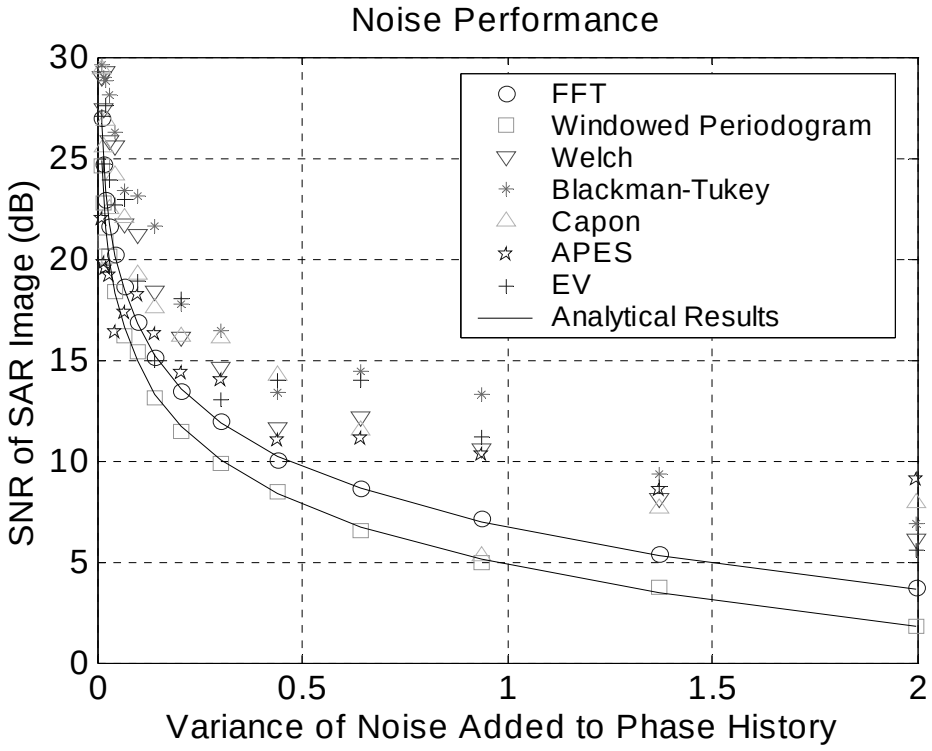

Figure 9. Signal to Noise Ratio (SNR) plotted vs. standard deviation of noise.

From this figure, it is clear that the Welch and Blackman-Tukey methods performed best, followed by the APES method. These results are expected again since the SNR is a function of the signal variance of which the Welch and Blackman- Tukey method set out to improve. The worst performers for signal to noise ratio was the Windowed Periodogram. This is due to the effect that a window has on the ability of the Periodogram to reduce the noise variance. Note again that in our simulations, the FFT method is equivalent to an un-windowed Periodogram. The APES method was best amongst the covariance-based methods at higher noise levels, approaching the performance of the Welch and Blackman-Tukey methods. In summary, all methods outperformed the Windowed Periodogram method.

3. Quadratic Phase Error Performance

Since SAR imagery is generated from a phase history, it is important to consider phase errors. These errors come mainly from errors in motion compensation between the sensor and the target, and are classified into low frequency, high frequency, and wideband groups. Each image formation method was evaluated against its resistance to low frequency quadratic phase errors only. Low frequency errors were chosen because they affect the mainlobe of the signal more so than the high and wideband errors. This introduces geometric distortion and reduced resolution [6]. It is important to assess how each image formation method reacts to varying levels of quadratic phase error because additional "auto focus" algorithms typically employed after image formation are only capable of compensating for a certain amount of phase error.

The quadratic phase error (QPE) was applied by multiplying the phase history by a phase error matrix. The same level of QPE was applied in both the horizontal and vertical dimensions of the phase history. A real SAR system, however, may experience different levels of phase error in each axis. The phase error matrix was created by the following expression:

(Eq. 29) $$\phi_{error} = e^{2\pi j\gamma(\frac{n}{N})^2} e^{2\pi j\gamma(\frac{m}{M})^2}$$

where

$$n = -N/2....N/2$$

$$m = -M/2....M/2$$

γ = Error in radians

Typically, a quadratic phase error of $\pi/4$ is considered acceptable and errors above $\pi/2$ are considered excessive [6]. The effect of QPE on a point target for these error levels can be seen below in Fig. 10. Clearly, the mainlobe width widens as the amount of error increases, thereby creating a loss in resolution. We will see how this affects the image quality on simulated data in Section V below.

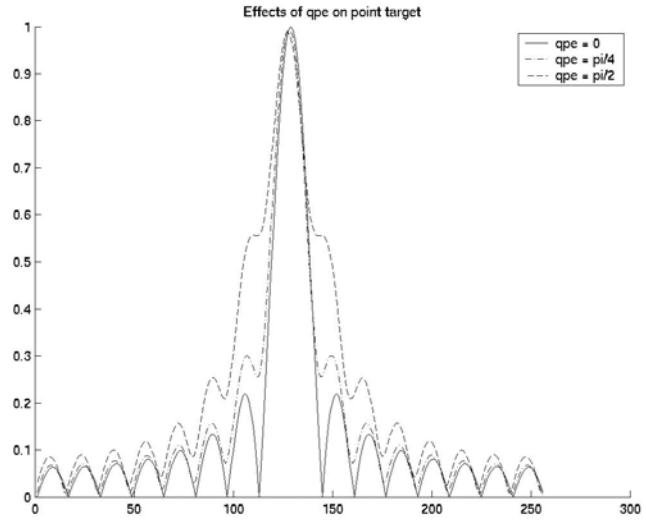

Figure 10. Quadratic Phase Error Effects On Point Target using FFT

To evaluate how each method responds to this error, the mainlobe width at one half the peak amplitude was determined for each method as the error was varied from 0 to 2π and applied to the phase history. The mainlobe width was chosen as a relative measure of resolution and is different from that in the previous section. The results are shown below in Figure 11.

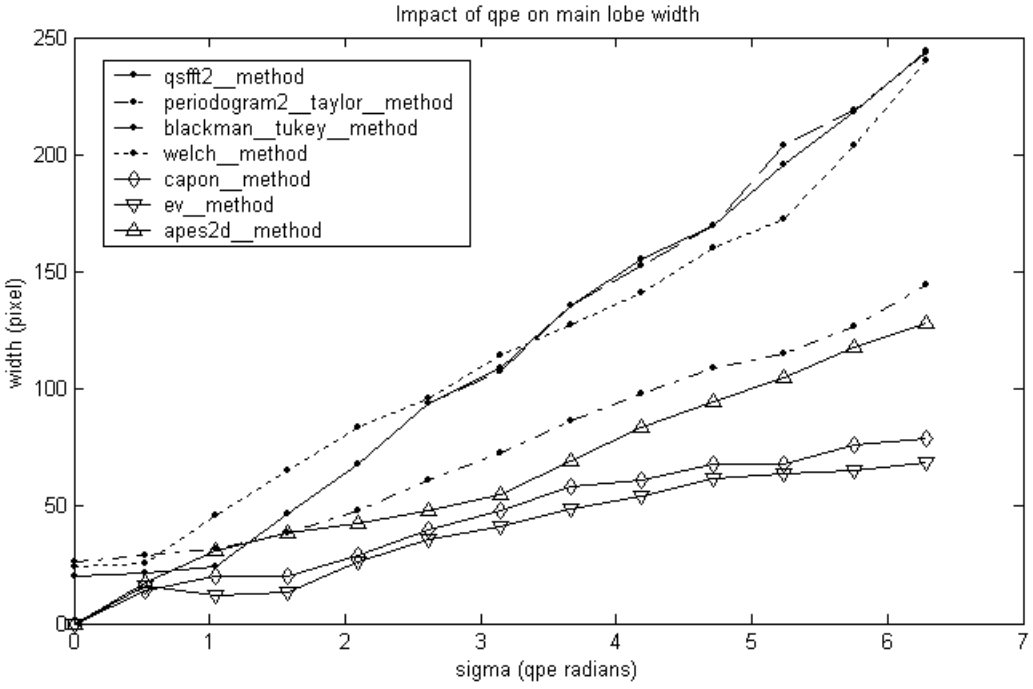

Figure 11. The change in the spatial resolution of various methods as a function of the severity of the quadratic phase error level. Spatial resolution is measured as the minimum number of pixels in between two point scatterers that results in a resolvable image. The sigma denotes the error in radians previously defined as gamma.

Fig. 11 shows that the width tends to increase linearly with σ. The three worst performing methods were the FFT, Blackman-Tukey, and Welch methods. The covariance-based methods out-performed the Periodogram-based methods because they start with a narrower mainlobe and are less affected by the widening caused by the QPE. The windowed Periodogram performed well because the windowing effect helped to combat the mainlobe widening caused by the QPE.

In general, for all methods except the Welch method, a quadratic phase error level less than $\pi/2$ keeps the width below 50 pixels. However, as the QPE increases to π, the performance of many methods degrade significantly, and there is no method with a width of less than 50. This is in accordance with the convention that quadratic phase errors of $\pi/4$ is considered acceptable and errors above $\pi/2$ are excessive.

V. Image Quality with Simulated Phase History Data

Understanding how each method performed quantitatively on just a few points provides the necessary background to evaluate and explain how each method performs on more elaborate data sets. In this section, image quality, effects of quadratic phase error, and computational complexity were evaluated using more complicated simulated phase history data.

1. Simulated Images

To simulate more realistic SAR data, we used the set of point scatterers shown in Fig. 12 (a). We generated a set of phase history data from this example, adding white Gaussian noise with variance 0.25. The size of the phase history data is 32 by 32, and the image size is 256 by 256. An image size larger then the phase history size is used to increase the number of frequencies evaluated to capture more detail. The spectral estimates of the image, given in Figs. 12 (b) through (h), can be used to discuss the advantages of using spectral estimation methods more complicated than the FFT or Periodogram.

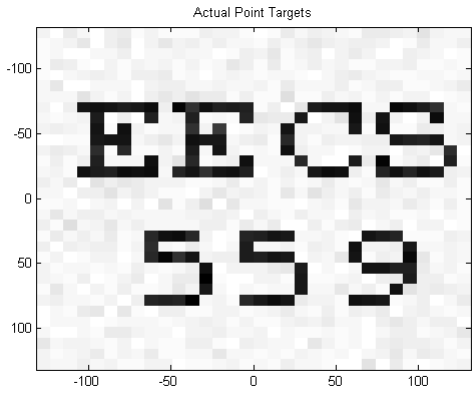

(a) Actual Point Targets

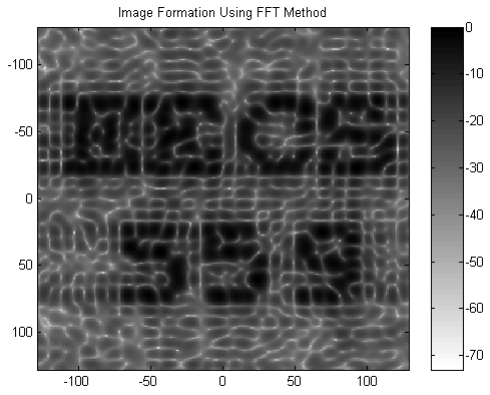

(b) FFT Method

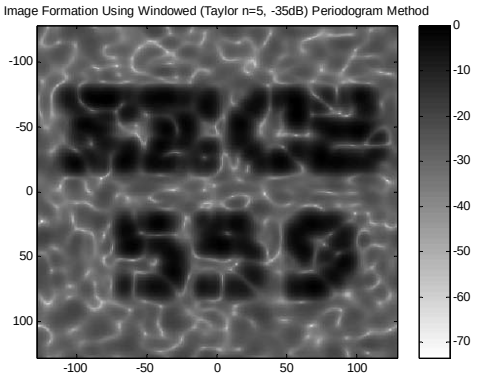

(c) Hamming Windowed Periodogram

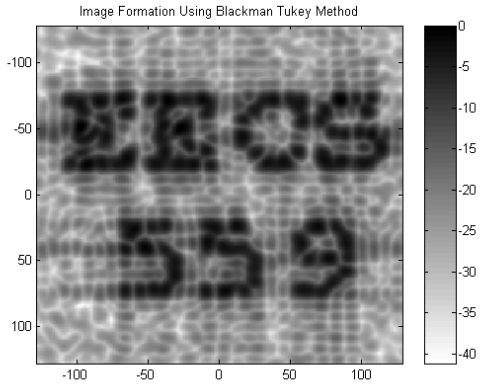

(d) Blackman-Tukey Method

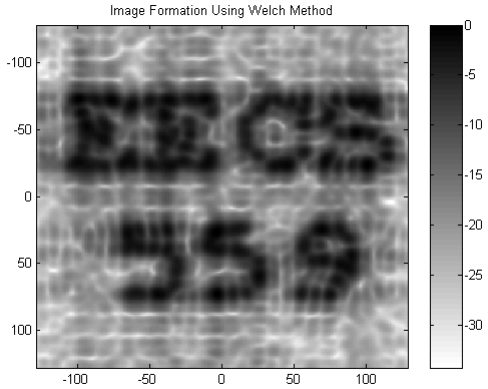

(e) Welch Method

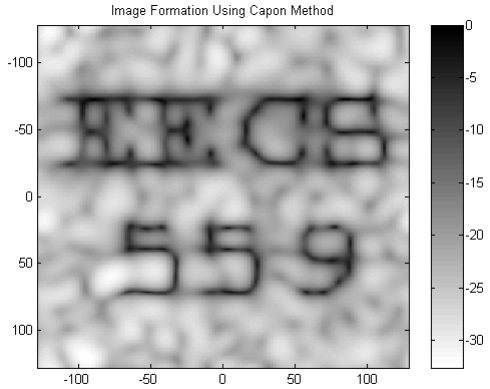

(f) Capon Method

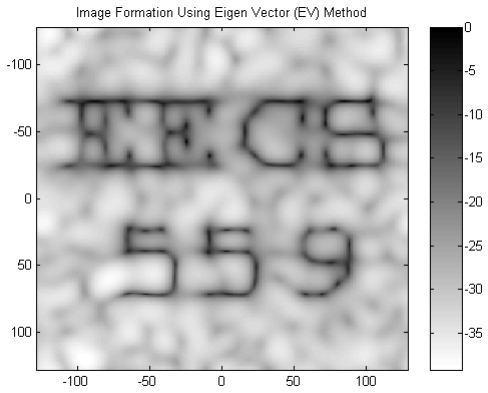

(g) EV Method

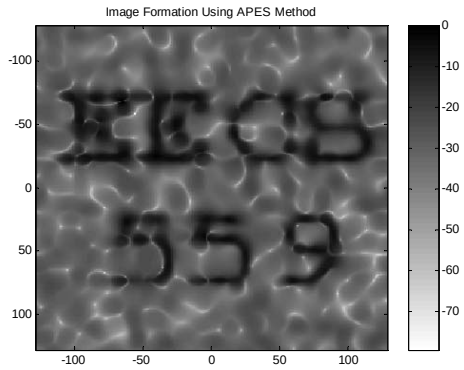

(h) APES Method

Figure 12. Images created by various methods using simulated phase history data

From the observation of the previous images, we can extract a few interesting characteristics from the different spectral estimators. The first group of estimators is composed of the Periodogram-based methods (Windowed Periodogram, Blackman-Tukey, and Welch methods). We know that these methods should give relatively poor resolution because of the increased size of the point target main lobe. However, they also help decrease the sidelobes, and therefore the points are more easily extracted from the background and noise when compared with the FFT method.

The second group of spectral estimators (Capon, EV, APES) can be used when a better resolution is needed. It appears that APES does not perform as well as the Capon or EV methods. However, the rationale for introducing the APES method was that it seems to give better estimates of the amplitude of the reflectivity function [3]. Since our simulations normalize amplitude, we can't confirm this.

2. Effect of Quadratic Phase Errors on Image Quality

To observe the subjective effects of quadratic phase error, images were created with varying degrees of phase error. The results in Figure 13 below show FFT and EV methods for QPE of $0, \pi/4$, and $\pi/2$. The FFT and EV methods were chosen because they were determined to be the worst and best performers against QPE based on the resolution analysis in Section IV. These images confirm the notion that a QPE greater then or equal to Pi/2 results in poor performance, while a QPE of Pi/4 still provides reasonable results. While these QPE's applied were deterministic, similar results are achieved by applying random QPE's.

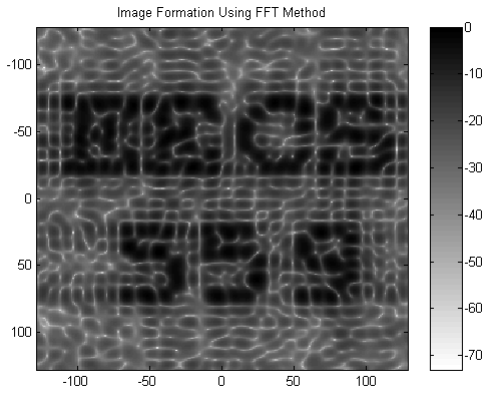

(a) FFT Method, QPE = 0

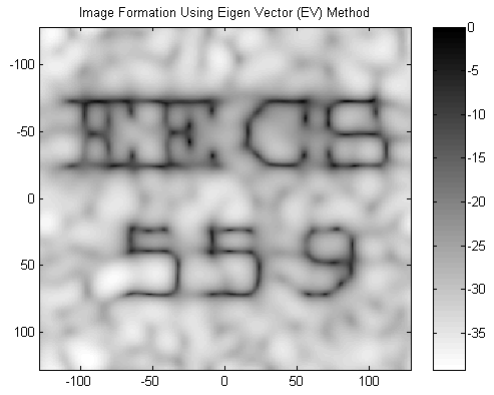

(b) EV Method, QPE = 0

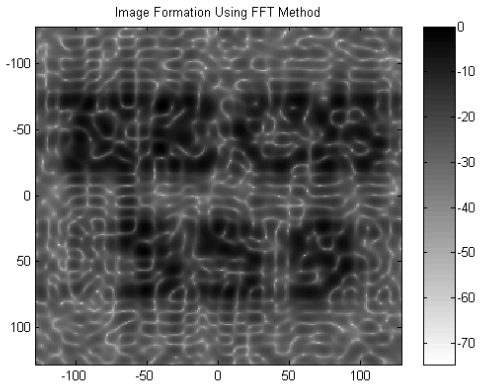

(c) FFT Method, QPE=Pi/4

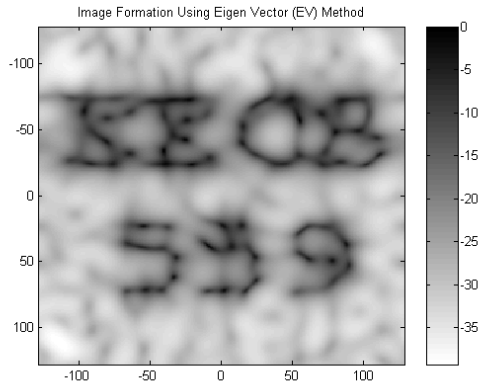

(b) EV Method, QPE = Pi/4

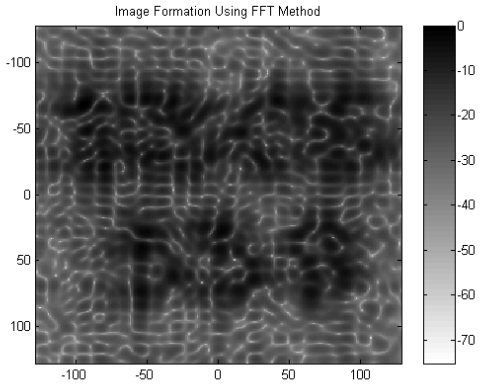

(e) FFT Method, QPE=Pi/2

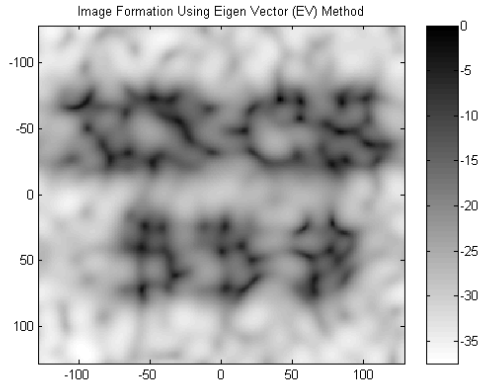

(b) EV Method, QPE =Pi/2

Figure 13. Simulated results for FFT and EV methods with 3 levels of quadratic phase error.

3. Computational Complexity

Although it was not an initial objective of this project, the computational complexity for some of the methods became an issue during simulations. Using the simulated data described above, the computation times for each method were determined in MATLAB. These are shown below in Table 2. These times were computed using a Sun Workstation running Unix with 2048MB of memory.

Method	Computation Time [sec]
FFT	0.1236
Windowed Periodogram	0.2319
Blackman Tukey	0.6223
Welch	17.5674
Capon	617.4787
EV	617.7149
APES	221.6561

Table 2: Comparison of Computation Times for Various Methods

Although the algorithms used were not optimized with respect to computation time, it is clear that the covariance-based methods require substantially more processing time than the FFT and Periodogram-based methods. This issue becomes even more critical when larger phase histories and images need to be processed, or if near real-time processing is required. Theoretically, the covariance based methods are on the order of $(K_x x K_y)^3$ computations while the Periodogram based methods exploit the efficient FFT which is of the order of $(NxM)\log(NxM)$. The APES method, however, was implemented using a fast algorithm that provided a threefold increase in processing time. Similar algorithms may be possible for the Capon and EV methods. Ultimately, the covariance methods are limited by the inversion or eigen decomposition of the autocovariance matrix.

VI. Image Quality with Actual Phase History Data

We were fortunate in this project to be able to use actual SAR phase history data collected by Veridian-ERIM International. This data was collected by the Data Collection System (DCS) air-to-ground X-band radar system mounted in a Convair CV-580 aircraft. The image is of the area around the University of Michigan football stadium. In this section, we describe the processing of this data and relate some issues that arise when using real phase history data. Then, our spectral estimators are applied to the data and the resulting images are shown.

1. Transitioning from Simulated to Real Data

Dealing with the much larger data set associated with actual SAR phase history data presented significant computation challenges. With a phase history size of

256 by 256 pixels, for most of the covariance-based methods, we estimated that a full covariance matrix, as described in Section III, would require more than 4 GB of RAM. This is beyond the capabilities of MATLAB and our network's best computers. To avoid that, we simplified the problem and used a smaller filter size instead of the typically recommended size of one half the phase history. Doing this sacrificed resolution, as can be seen comparing the results in Fig. 14 (a) and (b). In these two figures, the Capon method is applied to using a filter window of 1/16th and 1/8th the size of the phase history to see the improvement possible when doubling the filter size.

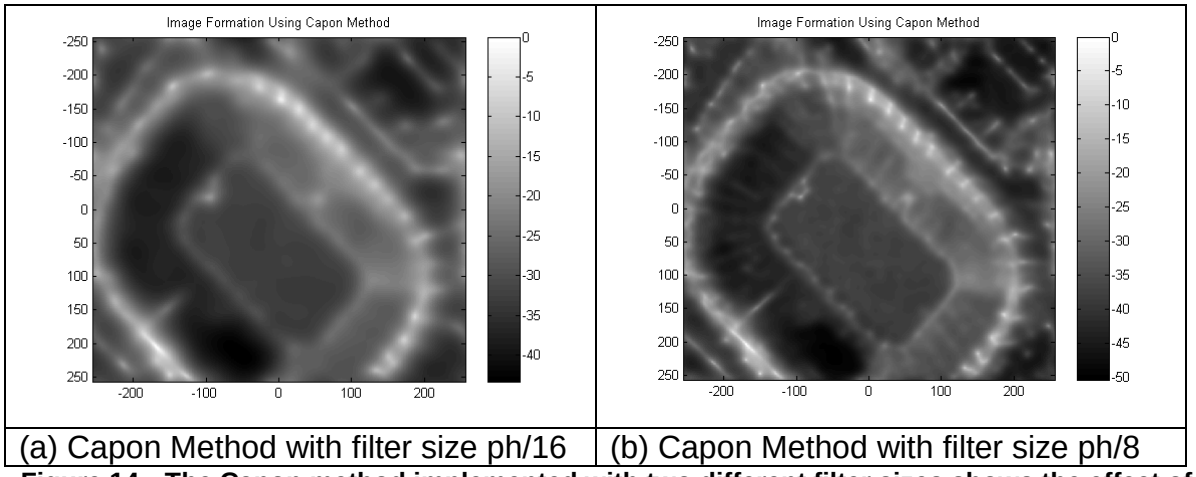

(a) Capon Method with filter size ph/16 (b) Capon Method with filter size ph/8

Figure 14. The Capon method implemented with two different filter sizes shows the effect of using more data in covariance-based methods. Here ph is the phase history size.

To achieve better resolution, the filter was reset to one half the phase history size and the data processing was performed in blocks which were later reconstructed to form the final image. Since the phase history could not be divided into blocks, an FFT was used to put the data in the image domain. From here it was divided into 16 blocks and an inverse FFT applied to return back to the phase history domain. This blocking process proved successful, however, artifacts of the block edges are apparent in the final images.

For the EV method, we explored the selection of model order with real SAR data, as we discussed briefly in Section III, part 3. The results are shown in Fig. 15. To speed up computation, a filter length of $M/32 = 8$ is used in the EV algorithm. This results in an R matrix dimension 81. Because of the narrow filter, the resolution is poor but still shows the effect of model order. As the model order increases, the 'pointiness' of the data increases. In fact, we can identify particular peaks that are emphasized as we move from Figure 15 (a) to (c). The model orders in (b) and (c) was chosen to include 95% and 98% of the signal energy in the signal subspace, respectively. We find that increasing the model order to 47 in Figure 15 (c) seems to brighten the image too much - some points that are clutter seem to have been emphasized.

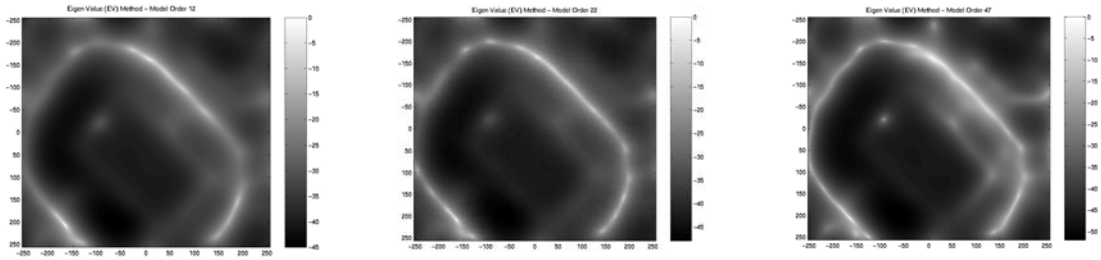

(a) (b) (c)

Figure 15. The UM stadium processed by the EV method with a model order of (a) 12, (b) 22, and (c) 47. The maximum model order possible in this simulation was 81. As the model order increases, more peaks can be seen in the image, but eventually noise in the image displays as peaks.

2. Final Images

Although we don't have an image of the 'actual' reflectivity for this area, we can still compare the results in Figure 16 (b) through (f) to see the differences between each method. Figure 16 (a) gives an indication of what the phase history of actual SAR image data we were provided looks like.

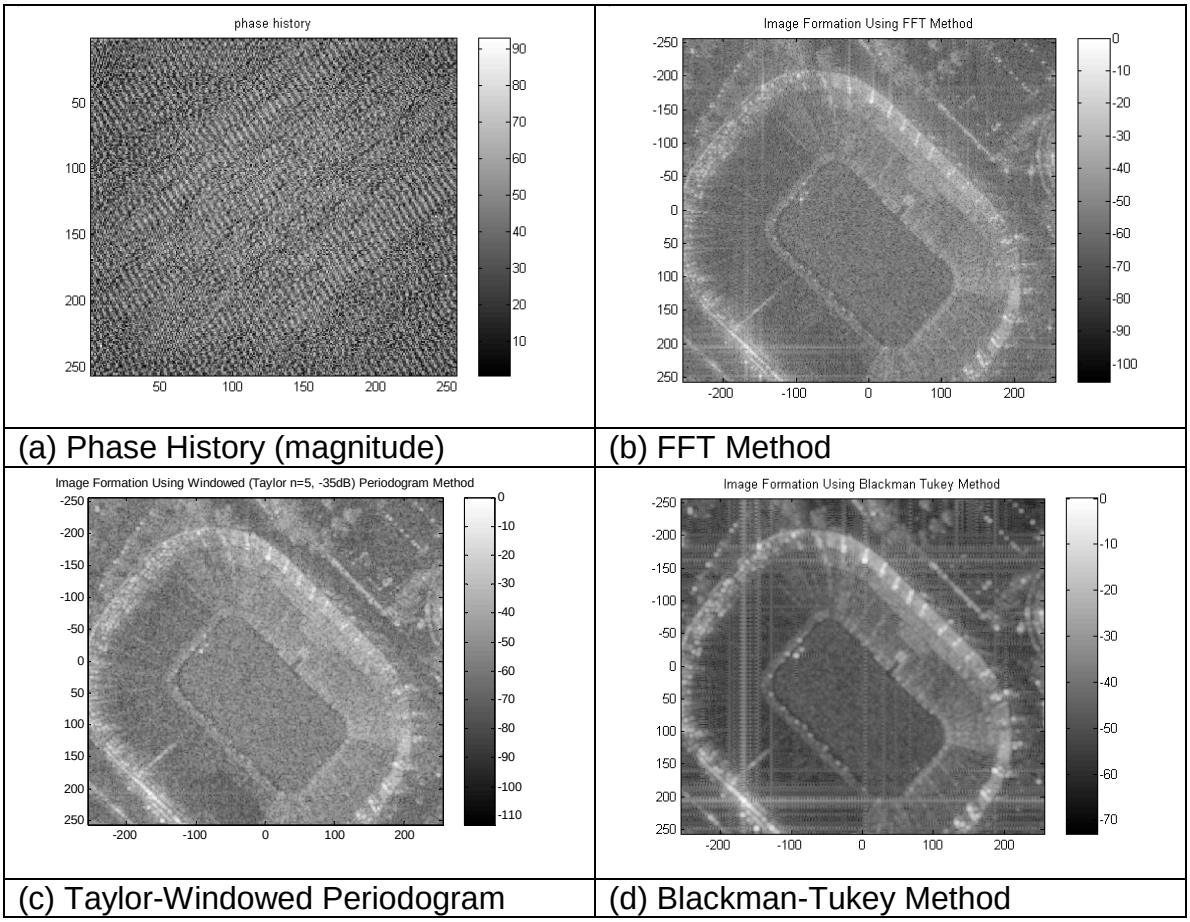

(a) Phase History (magnitude) (b) FFT Method

(c) Taylor-Windowed Periodogram (d) Blackman-Tukey Method

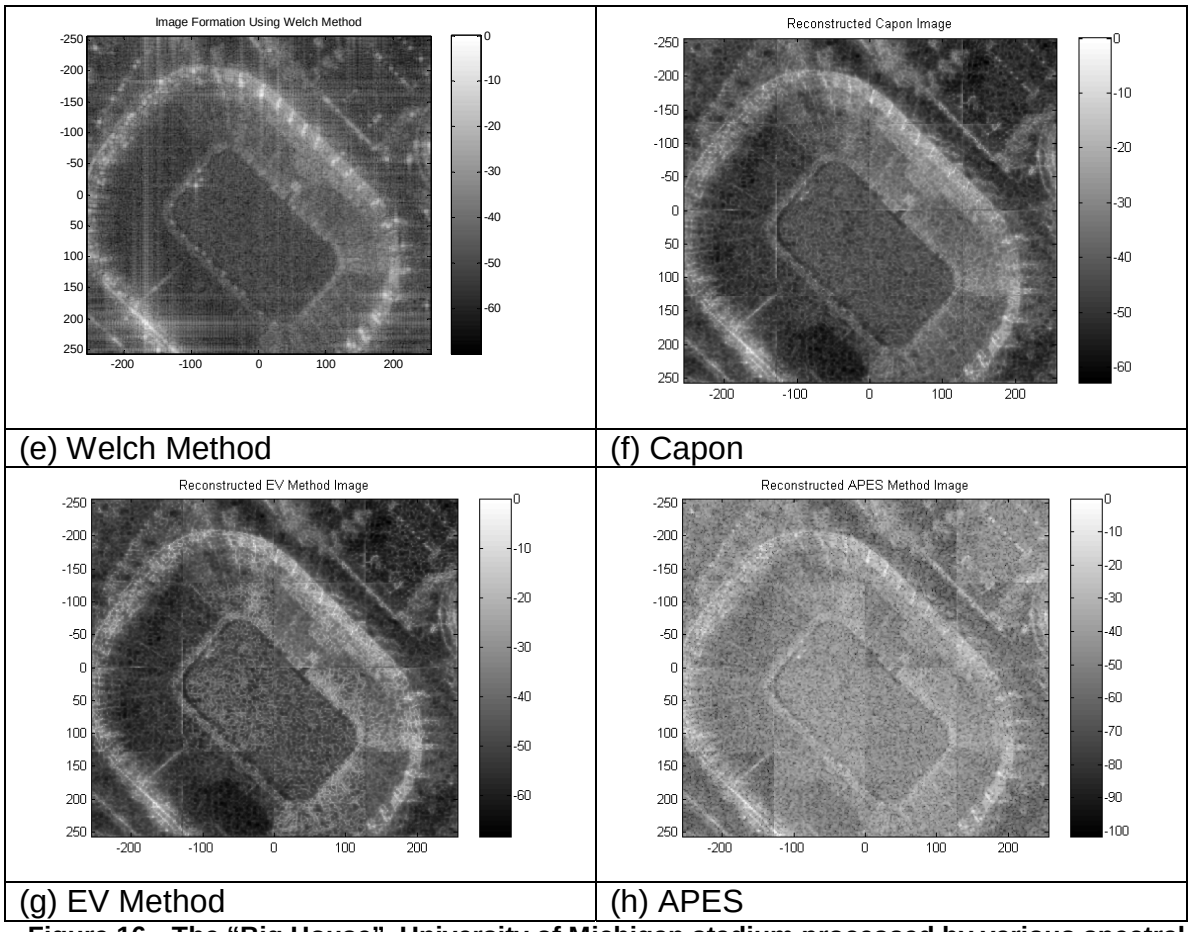

Figure 16. The "Big House", University of Michigan stadium processed by various spectral estimation techniques. Can you count the 110,000 seats?

Looking at the FFT method, we can see white horizontal and vertical lines. These are the sidelobes created by the high-amplitude peaks in the image. From close inspection we can see whole grids of these lines in the upper right corner. This is very different from the windowed Periodogram in (b), in which these sidelobe lines are virtually erased. Notice the noisy background of the windowed Periodogram. This noise is reduced by the Blackman-Tukey and Welch methods in (c) and (d), respectively, but the lines from the sidelobes return. These methods also seem to increase the contrast of the images. The Capon method, although processed in blocks, provides a low noise image with average resolution. The EV and APES results are similar to those of the Capon method.

In Section IV and V, the Capon, EV, and APES methods seemed to be vastly superior in terms of subjective image quality. These results using real data seem to contradict those results. It is likely that the wide range of intensities contained in the real data don't fit the assumption of sinusoids in noise that are central to the development of the covariance-based methods.

VII. Conclusion:

This project set out to explore various spectral estimation techniques that can be applied to SAR imaging systems. As we had little background in SAR, extensive research was conducted to understand the image formation process. This allowed us to accurately generate simulated data representative of the real SAR images to which we could apply the spectral estimation techniques once they were derived for the 2-D case.

The techniques used were grouped together based on their similarities with the Periodogram-based methods consisting of the Windowed Periodogram method, Blackman-Tukey method, and Welch method. Similarly, the remaining methods, Capon, EV, and APES were grouped together based on their extensive use of the autocovariance matrix. In the Periodogram based methods, the results show that the Welch and the Blackman-Tukey method do result in better noise performance at the cost of increased bias. Additionally, there seemed to be a clear benefit in using the Taylor window to reduce sidelobes. The covariance-based methods provided the best overall results on simulated data. This was based on resolution, MSE, and SNR criteria as well as subjective assessment of the simulated image data under various noise and phase error conditions. The subjective evaluation of the images revealed that resolution (or bias) has a larger effect on SAR image quality than noise variance does.

Finally, applying the spectral estimation techniques to actual SAR data revealed some surprises. The images created with the covariance-based methods did result in images without sidelobes and with subjective image quality equal to that of the Windowed Periodogram method, but they didn't have as much of a resolution advantage as we would have expected. The covariance-based methods also come at the price of significantly increased computational complexity and memory usage. While faster algorithms may be implemented, they are still limited by the inversion or eigen decomposition of the covariance matrix. This issue became critical when large data sets of actual phase history data was used.

Which method is best? It depends on the application. Based on the real data results, it is hard to beat the Windowed Periodogram. It is apparent that the covariance-based methods did not perform as well on actual data as they did on simulated data. Perhaps this indicates a departure from the model of a sum of sinusoids in noise. In particular, if the real scene is not just a set of point scatterers that produce a linear combination of complex exponentials, then the covariance-based methods will not perform as well as they did in the simulations [1].

Table 3 below summarizes our findings on the performance of various methods. Overall, these findings are inline with [1].

Method	Advantages	Disadvantages
FFT	Fast, simple	Large sidelobes
Windowed Periodogram	Fast, reduced sidelobes	Reduced resolution
Blackman Tukey	Good noise performance	Large sidelobes
Welch	Good noise performance	Poor Resolution
Capon	High resolution	High computational complexity, medium results w/ actual data
EV	High resolution	High computational complexity, medium results w/ actual data
APES	High resolution, faster than Capon or EV	High computational complexity, medium results w/ actual data

Table 3: Summary of Characteristics of Each Method

Overall, this project provided great insight into issues associated with applying theoretical solutions to real engineering problems. This basic understanding will be helpful in applying more advanced signal processing techniques in our future careers.

Lastly, the authors wish to thank Veridian-ERIM International for providing the actual SAR data for use in our analysis.

VIII. References

[1] DeGraaf, S. R. "SAR Imaging via Modern 2-D Spectral Estimation Methods", *IEEE Transactions on Image Processing*, Vol. 7, No. 5, May 1998, pp. 729-761.

[2] Stoica P. and Moses R. *Introduction to Spectral Analysis*. Prentice Hall, Upper Saddle River, NJ, 1997.

[3] Li, J. and Stoica P. "An Adaptive Filtering Approach to Spectral Estimation and SAR Imaging", *IEEE Transactions on Signal Processing*, Vol. 44, No. 6, June 1996, pp. 1469-1484.

[4] Oliver, C. and Quegan, S. *Understanding Synthetic Aperture Radar Images.* Artech House, Boston, 1998.

[5] Munson, D.C., Jr. and Visentin, R.L. "A signal processing view of strip-mapping synthetic aperture radar **"**, *IEEE Transactions on Acoustics, Speech and Signal Processing*, Vol. 37, No. 12, Dec. 1989, pp. 2131 –2147.

[6] Carrara, W.G., Goodman, R.S., Majewski, R.M. "*Spotlight Synthetic Aperture Radar-Signal Processing Algorithms* **"**, Artech House, Norwood, MA, 1995.

[7] Kay, Stephen M. *Modern Spectral Analysis*. PTR Prentice Hall, Upper Saddle River, New Jersey, 1988.

[8] Jakobsson, A., Marple, L. Jr., and Stoica, P. "Computationally Efficient Two-Dimensional Capon Spectrum Analysis," *IEEE Transactions on Signal Processing*, Vol. 48, No. 9, Sept 2000, pp. 2651-2661.

[9] Capon, J. "High Resolution Frequency-Wavenumber Spectrum Analysis", *Proceedings of the IEEE*, Vol. 57, Aug. 1969, pp. 1408-1418.

[10] Liu, Z-S, Li, H, and Li, J. "Efficient Implementation of the Capon and APES for Spectral Estimation", *IEEE Transactions on Aerospace and Electronic Systems*, Vol. 34, No. 4, Oct. 1998, pp. 1314-1319.

[11] Jakowatz, C., et al, *"Spotlight-Mode Synthetic Aperature Radar: A Signal Processing Approach"*, Kluwer Academic Publishers, Boston, MA, 1996.